

Article

Particle-Size Fractionation and Thermal Variation of Oil Shales in the Songliao Basin, NE China: Implication for Hydrocarbon-Generated Process

Jianliang Jia ^{1,*}  and Zhaojun Liu ²¹ Institute of Geology, Chinese Academy of Geological Sciences, Beijing 100037, China² College of Earth Sciences, Jilin University, Changchun 130061, China; liuzj@jlu.edu.cn

* Correspondence: jiajianliang@cags.ac.cn or jiajl0228@163.com

Abstract: The synchronous variation and association of organic matter (OM) and minerals in the hydrocarbon-generated process of oil shales are poorly understood. The goal of the paper is to investigate OM occurrence and thermal variation so as to reveal the hydrocarbon generation potential of oil shales. Based on detailed analyses of particle, organic, mineral, and thermal data from lacustrine oil shales in the Songliao Basin, we observed three layers of shale particles after settling in the water column characterized by a distinct color, degree of consolidation, and particle size. The particle sizes are divided into three ranges of fine grain (<1 μm), medium grain (1–20 μm), and coarse grain (>20 μm) via laser particle analysis. The particle-size distribution indicates the presence of OM polymerization and dominant contribution of the associated mineral surface and bioclastic OMs to the OM abundance of oil shale. Various OM occurrences are influenced by OM sources and redox conditions, whereas the degree of biodecomposition and particle sizes affect the placement of OM occurrences. Based on multiple thermal analyses, a synchronous response of OM and minerals to thermal variation dominates at 300–550 °C. The I/S and chlorite minerals are characterized by an entire illitization, while solid/absorbed OMs and hydrocarbon-generated water were expelled in large quantities. This contributes to major loss weights of oil shales during heating. The peak hydrocarbon-generated rate occurred at 457 °C for oil shales, corresponding to around 1.3% vitrinite reflectance value. These results are suggested to improve the understanding of OM occurrences and the thermal degradation constraint on the hydrocarbon-generated process, and contribute to the interpretation of the hydrocarbon generation potential and in-situ exploitation of oil shales.



Citation: Jia, J.; Liu, Z. Particle-Size Fractionation and Thermal Variation of Oil Shales in the Songliao Basin, NE China: Implication for Hydrocarbon-Generated Process. *Energies* **2021**, *14*, 7191. <https://doi.org/10.3390/en14217191>

Academic Editor: Reza Rezaee

Received: 28 September 2021

Accepted: 25 October 2021

Published: 2 November 2021

Keywords: oil shale; particle fractionation; thermal variation; hydrocarbon-generated process

Publisher's Note: MDPI stays neutral with regard to jurisdictional claims in published maps and institutional affiliations.



Copyright: © 2021 by the authors. Licensee MDPI, Basel, Switzerland. This article is an open access article distributed under the terms and conditions of the Creative Commons Attribution (CC BY) license (<https://creativecommons.org/licenses/by/4.0/>).

1. Introduction

Organic matter (OM) and minerals are major components for oil shales and interact with each other during the process of sedimentation and diagenesis [1]. Only 10% of the OM in argillaceous sediments is isolated OM without the influence of clay minerals [2–6], whereas more than 80% of OM is closely related to clay minerals, and most of it exists in the form of organic-clay complexes with the advantage of soluble OM [7–9]. The mineral-associated OM is the main form of OM occurrences in fine-grained sediments [10,11]. During sedimentation, the sorption of OM to the surface of mineral particles governs the fate of OM [12–15]. Various types of OM (e.g., organic debris, aggregated OM, sorbed OM) based on physical and chemical properties have been observed [16]. These OM occurrences have been proposed to be derived by their interaction with minerals during deposition and diagenesis [17]. In general, OM distribution associated with minerals is evidenced in the clay-sized fraction of shales [1,14,18]. However, a lack of knowledge exists regarding OM occurrence and its genesis for whole rocks [19,20], particularly with respect to organic-rich oil shales.

Oil shale and shale oil regarded as two unconventional oil and gas resources with huge potential worldwide attracted significant attention recently [21–24]. The in-situ exploitation of oil shale [25,26] and the resource potential of shale oil [27,28] are closely related to the hydrocarbon-generated process of organic-rich shales in different sedimentary settings. Hereby, it is very important to reveal the variation and association of OM and minerals in the hydrocarbon-generated process of oil shales. A series of studies were carried out on the hydrocarbon-generated process associated with thermal degradations for oil shales of various types [29–32]. The variations of organic products [30–32] or minerals [33,34] were primarily focused after the heating of oil shales. Nevertheless, OM occurrences are strongly linked with minerals during deposition and diagenesis [7–18], and their associations can be observed by SEM-BSE micrographs [18,35]. The synchronous process of OM decomposition, mineral transformation, and water release occurring in shales was verified by previous studies [14,36–41]. This also could exist in the process of thermal evolution [42,43] or the in-situ production for oil shales [29–34]. However, the influence of the association between OM and minerals on the hydrocarbon-generated process during the heating of oil shales is poorly understood. Consequently, more data need to be gathered about thermal variation related to various OM and minerals.

The purpose of this study is to examine the relationships between OM occurrence, thermal variation, and the hydrocarbon-generated process of oil shales through integrated particle, organic, mineral, and thermal analyses. This study would illustrate the importance of examining the association between OM and minerals to interpret the hydrocarbon-generated process of oil shales, which contributes to the hydrocarbon generation potential and in-situ exploitation of oil shales.

2. Materials and Methods

2.1. Materials

The Songliao Basin is the largest oil- and gas-prone non-marine rift basin in NE China, which covers an area of about 26×10^4 km² (Figure 1a) [44,45]. The sediments are dominated by Cretaceous terrigenous successions (Figure 1a) [46]. Oil shales were mainly deposited in Qingshankou (K₂qn) and Nenjiang formations (K₂n) during the Upper Cretaceous period (Figure 1b) [45–47]. Samples were taken from borehole Ngn2 and ZK3389, located in the southern basin (Figure 1a). Two boreholes revealed the Qingshankou (Ngn2; Figure 2a) and Nenjiang (ZK3389; Figure 2b) formations, developing excellent oil shales with a predominance of kerogen Type-I and -II₁ [47].

We studied the oil shales hosted in the semi-deep to deep lacustrine deposits in Member 1 of the Qingshankou (K₂qn₁) and Members 1 and 2 of the Nenjiang (K₂n₁₋₂) formations (Figure 2a,b). A major contribution of aquatic organisms to OM accumulation occurred in the K₂qn₁ and K₂n₁₋₂ deposition [45,46]. A total of 141 samples from boreholes Ngn2 (~91) and ZK3389 (~50) were selected for total organic carbon (TOC) and Rock-Eval analyses (Figure 2). Hereby, we preferred to choose target samples with different TOC contents and a similar OM type and maturity among oil shales and mudstones, so as to reveal the hydrocarbon-generated process and potential of oil shales. In particular, samples with low carbonate minerals were selected to investigate the effect of clay minerals on OM occurrence and thermal variation. A wide range of data was selected for particle setting (~8), laser particle size (~12), microscopic inspection (~24), thermogravimetry (TG)-differential scanning calorimetry (DSC) (~5), X-ray diffractometry (XRD) (~4), gas chromatography-mass spectrometry (GC-MS) (~43), and pyrolysis-gas chromatography (Py-GC) (~6) analyses (Figure 2a,b).

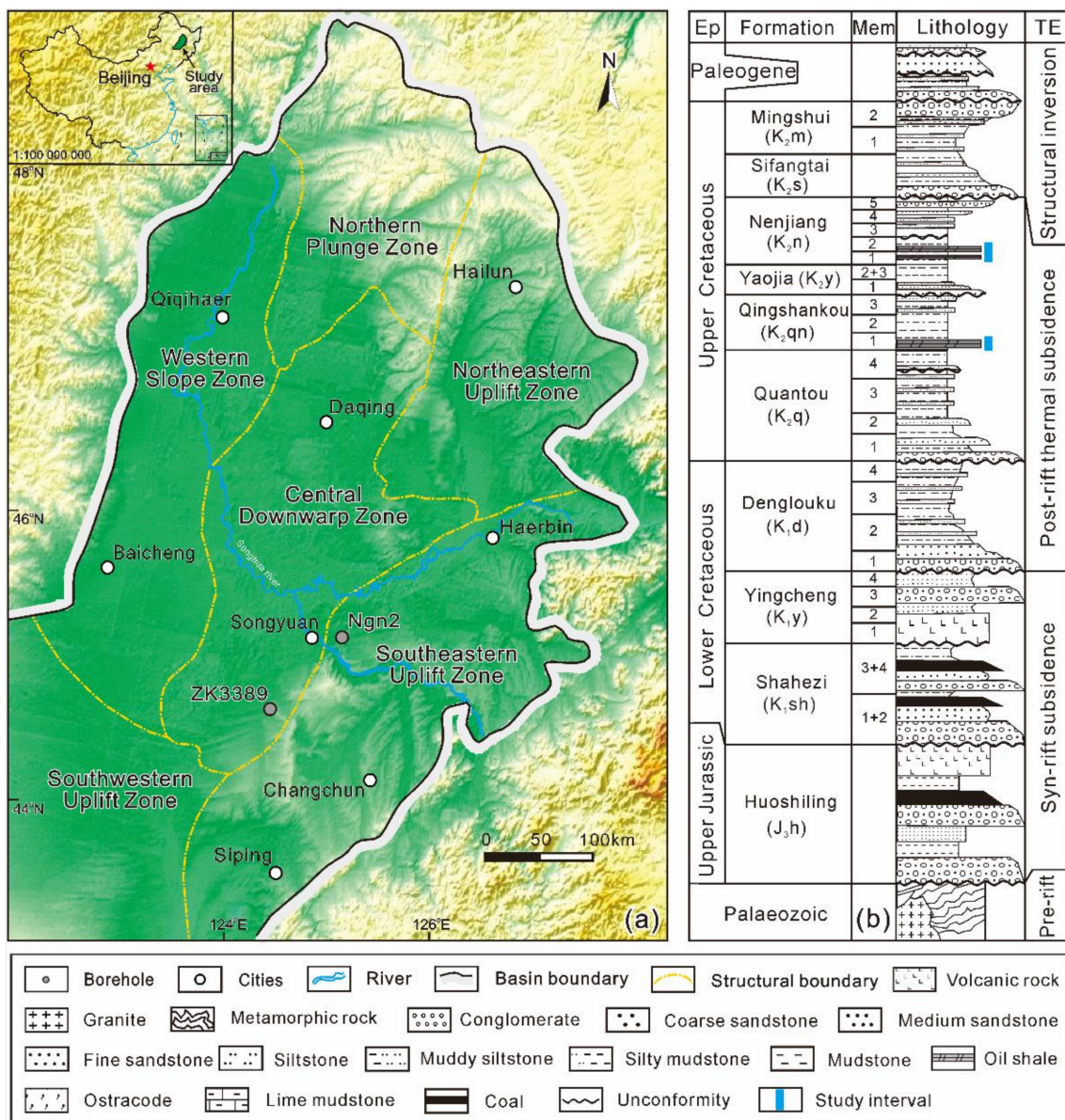


Figure 1. Structural units with its location map (after [45]) (a), and the generalized stratigraphic column of the Songliao Basin (after [44,45]) (b), exhibiting the location of boreholes Ngn2 and ZK3389. Ep = epoch, Mem = member, TE = tectonic evolution.

2.2. Methods

Particle fractionation for sediments is an effective method to probe into the distribution of particle sizes and OM. The grain size separation of pulverized samples (≤ 200 mesh) was obtained by the sinking method based on Stocks Law at the Beijing Research Institute of Uranium Geology, China. Dispersed particles were treated by the addition of 5% HCl and repetitive ultrasonic leaching. Three distinct layers formed after a four-day sinking of samples in the water column. The lower layer formed within 0.5–1.0 h was separated from the suspension liquid, dried in an oven at 35 °C, and weighted (M1; Table 1). After ~8 h of standing of the above suspension liquid, the grain size fraction in the suspension within the top 10 cm of the column (upper layer, M3; Table 1) was collected. The remaining particles were taken as the middle layer (M2; Table 1). The analytical precision for all samples is estimated to be $\leq 4.4\%$ according to the weight loss (Table 1).

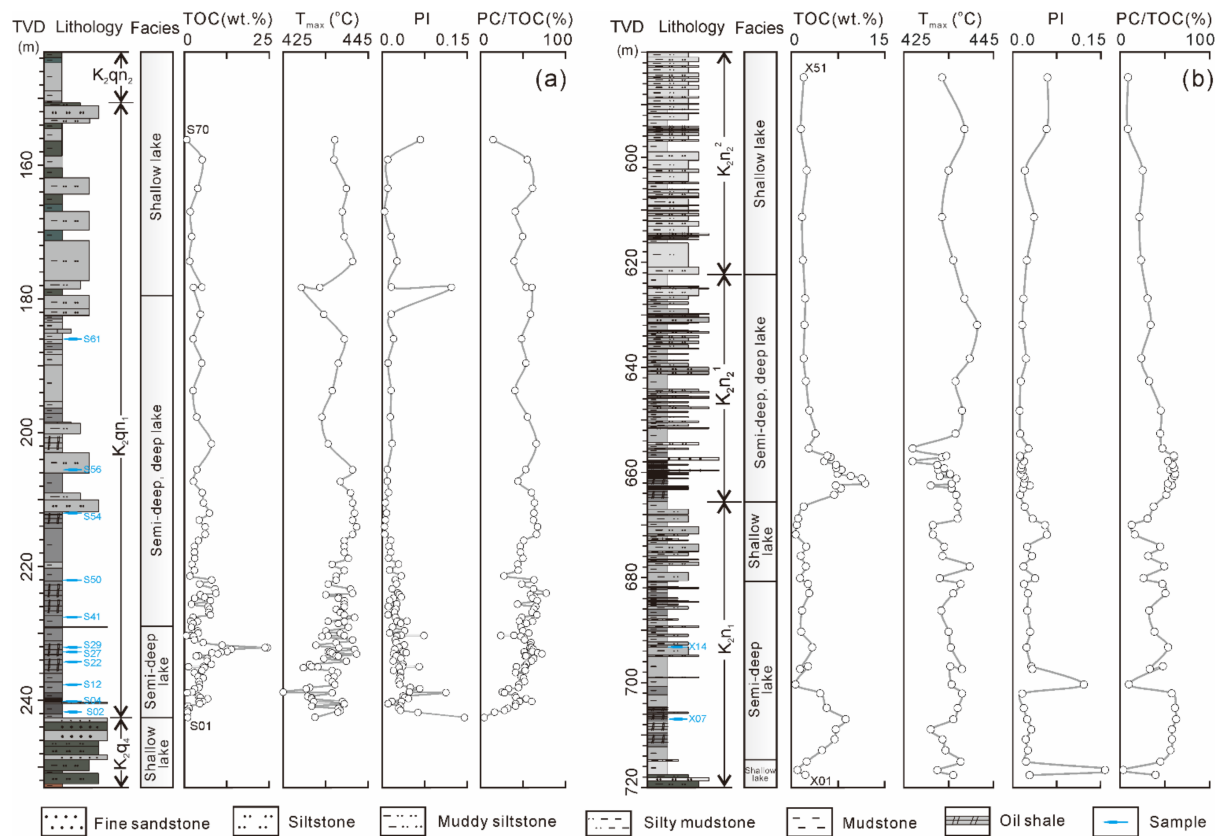


Figure 2. Lithologic profiles and sedimentary facies with position of measured samples from boreholes Ngn2 of the K_2qn_1 (a) and ZK3389 of the K_2n_{1-2} (b) in the Songliao Basin, showing TOC contents, T_{max} values, PI values, and PC/TOC ratios from two boreholes. TVD = true vertical depth.

Table 1. Layer-specified parameters of grain size fractions from lacustrine oil shales and mudstones in the K_2qn_1 .

Layer	Sample	S02	S04	S22	S27	S29	S50	S56	S61
Lower	Weight M_1 (g)	1.97	2.82	5.12	6.63	7.71	5.53	4.20	3.33
	Layer-specified TOC ¹ (wt.%)	0.03	0.73	1.93	5.66	9.96	2.82	0.86	0.42
	Layer-specified S1 (mg/g)	0.01	0.06	0.22	0.91	1.92	0.38	0.05	0.03
	Layer-specified S2 (mg/g)	0.06	6.13	14.38	40.12	56.91	20.53	6.34	1.18
Middle	Weight M_2 (g)	8.72	6.33	7.54	10.14	10.95	7.92	5.28	10.21
	Layer-specified TOC (wt.%)	0.20	1.33	2.53	7.54	13.72	3.91	1.00	1.42
	Layer-specified S1 (mg/g)	0.02	0.10	0.27	1.05	2.58	0.44	0.06	0.07
	Layer-specified S2 (mg/g)	0.30	11.40	18.58	58.80	80.67	28.44	7.24	3.88
Upper	Weight M_3 (g)	8.65	10.45	6.63	2.73	1.13	4.75	9.85	3.80
	Layer-specified TOC (wt.%)	0.41	3.07	2.65	1.31	0.83	2.34	2.26	0.40
	Layer-specified S1 (mg/g)	0.06	0.23	0.34	0.18	0.09	0.28	0.13	0.03
	Layer-specified S2 (mg/g)	0.97	25.11	19.51	9.46	5.09	16.67	16.19	1.42
Error	Cumulative TOC (wt.%)	0.64	5.13	7.10	14.50	24.51	9.05	4.12	2.23
	Whole-rock TOC (wt.%)	0.65	5.36	7.07	14.50	24.40	8.68	4.06	2.14
	Analytical precision (%)	1.72	4.29	-0.47	0.00	-0.44	-4.26	-1.67	-4.39

¹ Total organic carbon.

The total organic carbon (TOC) for pulverized samples (≤ 200 mesh) was measured with a LECO-CS230 elemental analyzer on samples pre-treated with concentrated HCl (5%) for 6 h to remove the inorganic carbon. An aliquot of 100 mg for each sample is used and combusted at an oven temperature of ca. 1100 °C, where the released CO₂ is measured through an infrared cell with an analytical precision better than 0.2 wt.%. Pyrolysis for pulverized samples (≤ 200 mesh) was carried out using a Vinci Rock-Eval 6 instrument. Around 60 mg of the powdered sample was placed into a crucible using a funnel. Then,

the quantity of pyrolyzate (S1, S2, mg HC/g rock; S3, mg CO₂/g rock) generated from the kerogen during gradual heating (S1, 300 °C for 3 min; S2 and S3, 650 °C with a rate of 25 °C min⁻¹) in a helium stream was normalized to TOC to give the hydrogen index (HI = 100 × S2/TOC, mg HC/g TOC), production index (PI = S1/(S1 + S2)), and pyrolytic available carbon (PC = 0.083 × (S1 + S2)). The temperature of maximum hydrocarbon generation (T_{max}) serves as a maturation indicator. Bulk parameters from specified layers were also obtained by Leco and Rock-Eval analyses after drying and crushing (≤200 mesh). TOC and pyrolyzate (S1, S2) values of each layer are calculated from Leco and Rock-Eval pyrolysis results multiplied by the corresponding weight percentages (Table 1). All of the above tests were measured at the Center for Scientific Test of Jilin University, China.

The distribution of particle sizes for whole rock samples (≤200 mesh) was obtained by a laser diffraction analyzer (Horiba LA-950) with a measuring range of 0.02–2000 μm at the Beijing Center for Physical and Chemical Analysis, China. Particle-free water or particle-free solution saturated with a drug were used as dispersants. The pretreated sample was put into a water-filling tank forming a suspended solution by ultrasonic and mechanical dispersion. The suspended particle flow by a pump drive passing through the laser beam occurred with diffraction, which was recorded by a detector on the detection board. The final result was calculated and output was created by a computer with analytical precision better than 2%. Microscopic inspection for layer-specified samples was conducted for petrographic characters of OM and minerals from each layer by thin and polished sections. The curves of thermal changes for the whole rock and layer-specified samples were obtained by a thermogravimetry (TG)-differential scanning calorimetry (DSC) analysis at the Analytical Instrumentation Center of Peking University, China. The powder sample (≤200 mesh) was put into the platinum crucible, and then the crucible was put on the DSC-c_p highest accuracy sample holder in the furnace. This was carried out in the temperature range of 20–800 °C with a temperature ramp of 10 °C min⁻¹ using a nitrogen atmosphere. During the heating process of each run, the mass change and calorimetric effects were recorded. Then, the TG and DSC curves can be obtained.

Changes in mineral phases were conducted in pulverized samples (≤200 mesh) via X-ray diffraction (XRD) using a D/MAX-2400 instrument at the Institute of Geology and Geophysics of the Chinese Academy of Sciences in Beijing, China. The natural oriented (N, suspension for air drying), ethylene glycol-saturated (EG at 60 °C for 8 h), and high temperature (T 150 °C, T 450 °C, T 500 °C, and T 550 °C for 2.5 h) sections were prepared from the suspension liquid of the samples. Each sample was pulverized to 200 mesh and pressed smoothly into a glass groove to obtain a pressed pellet, which generated a wide-angle curve after XRD (CuKα = 1.54184 Å). We identified each mineral at diffraction angles (2θ) ranging from 3 to 15° using characteristic peaks based on different crystal lattice spacings (d). The relative percentages of minerals were calculated using the areas of the diffraction peaks.

Gas chromatography-mass spectrometry (GC-MS) and pyrolysis-gas chromatography (Py-GC) analyses were measured at the Department of Applied Geosciences and Geophysics of Montanuniversität Leoben (Austria). The saturated hydrocarbon fractions were analyzed on a gas chromatograph equipped with a 30 m DB-5MS fused silica capillary column (i.d. 0.25 mm; 0.25 μm film thickness) and coupled to a Finnigan MAT GCQ ion trap mass spectrometer [45–47]. The oven temperature was programmed from 70 °C to 300 °C at a rate of 4 °C min⁻¹, followed by an isothermal period of 15 min. Helium was used as the carrier gas, and the sample was not split and was injected at 275 °C. The mass spectrometer was operated in the EI (electron impact) mode over a scan range from m/z 50 to m/z 650 (0.7 s total scan time). Data were processed with a Finnigan data system. Identification of individual compounds was accomplished based on retention time in the total ion current (TIC) chromatogram and a comparison of the mass spectra with published data. Py-GC analyses were carried out using the Quantum MSSV-2 Thermal Analysis System [48]. Thermally extracted (300 °C for 10 min) whole rock samples (≤200 mesh) were heated in a flow of helium, and products released over the temperature range 300–600 °C (40 K min⁻¹)

were focused using a cryogenic trap, and then analyzed using a 50 m × 0.32 mm BP-1 capillary column equipped with a flame ionization detector. The GC oven temperature ranged from 50 °C to 300 °C at 10 °C min⁻¹. The major components were identified and quantified by external standardization using *n*-butane, including boiling ranges (C₁, C₂₋₅, C₆₋₁₄, C₁₅₊) and individual compounds (*n*-alkenes, *n*-alkanes, alkylaromatic hydrocarbons, and alkylthiophenes).

3. Results

3.1. Bulk Parameter

The gray brown, black gray, and dark grey oil shales (Figure 3a) were developed in a semi-deep to deep lacustrine environment during the K₂qn₁ and K₂n₁₋₂ periods (Figure 2). The TOC content of oil shales varies between 5.13 and 24.51 wt.% (avg. 8.15 wt.%) (Figure 2a,b), whereas a low TOC content (0.64–4.94 wt.%, avg. 2.66 wt.%) is obtained from mudstones in the K₂qn₁ and K₂n₁₋₂ (Figure 2a,b). Overall low T_{max} values (425–443 °C) were present in oil shales and mudstones (Figure 2a,b), indicating immaturity to low maturity around 0.5% vitrinite reflectance value. The production index (PI) values (0–0.19, avg. 0.03) are low in oil shales and mudstones of the K₂qn₁ and K₂n₁₋₂ (Figure 2a,b), due to low OM maturity. However, relatively high PI values of oil shale intervals were present in the lower K₂qn₁ and K₂n₁₋₂ (avg. 0.05) (Figure 2a,b), reflecting a higher hydrocarbon potential for oil shales. In addition, higher degradation ratios ($D = PC/TOC$, PC = Pyrolytic available carbon) occur in oil shale intervals (avg. 61.8%) compared with that of mudstones (avg. 41.8%) (Figure 2a,b), indicating an enhanced efficiency of hydrocarbon generation for oil shales.



Figure 3. Settling layer-specified character for pulverized oil shales and mudstones from borehole Ngn2, exhibiting photographs of borehole cores (a), grain size separation in the water column for pulverized shales (b), and the powders of layer-specified particles (c).

3.2. Distribution of Particle Sizes

The size of powder particles from oil shales and mudstones in the K₂qn₁ and K₂n₁₋₂ is divided into three ranges of particle sizes, including fine grain (<1 μm), medium grain (1–20 μm), and coarse grain (>20 μm), in which the abundance of medium grains dominates (Figure 4a). TOC content shows a positive correlation with median sizes of all particles ($r^2 = 0.96$) (Figure 4b), implying the effect of OM polymerization on particle sizes. However,

the abundance of particle sizes for oil shales and mudstones exhibits a variation with changing TOC contents (Figure 4a). The increased (0.6–4.1 wt.% TOC) and then decreased particle-size abundances (5.1–24.5 wt.% TOC) with enhancing TOC contents are observed in fine grains (Figure 4a), indicating reduced fine grains due to high OM abundance (TOC >5.0 wt.%). The abundance of medium grains decreased with the increase in TOC content, whereas an increase in TOC content enhanced the abundance of coarse grains (Figure 4a).

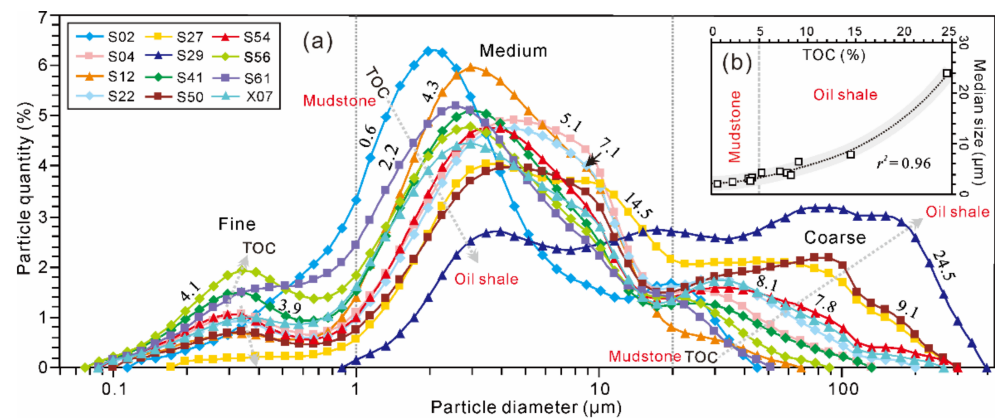


Figure 4. The distribution of laser particle sizes for pulverized samples from boreholes Ngn2 and ZK3389 (a), and the relationship between TOC contents and median sizes (b).

3.3. Particle-Size Fractionation

3.3.1. Settling Layer-Specified Character

After the settling of the particles from oil shales and mudstones in the water column, three layers are obvious, characterized by a distinct color, degree of consolidation, and particle size (Figure 3b,c). The settling velocity of the particles is controlled by particle size and bulk density based on Stocks Law. In general, the lower layer is characterized by grey black, large particles of detrital minerals, and granular OM (Figure 5a). The middle layer contains dark grey, consolidated particles of small grain size (dominant clays), and particulate OM (Figure 5b). Highly consolidated grey and fine-grained materials, containing predominant fine clays and soluble OM, are present in the upper layer (Figure 5c). However, smaller particles may contain some fine detrital minerals (Figure 5b,c), while larger particles may also be mixed with partially organic-clay aggregates (Figure 5b,c).

3.3.2. Layer-Specified OM Distribution

Different relationships are found between layer-specified TOC, pyrolyzate (S1, S2) data, and whole-rock TOC contents (Figure 6). For lower and middle layers, layer-specified TOC contents increase with increasing whole-rock TOC contents (Figure 6a), whereas in the upper layer TOC contents increase up to whole-rock TOC <5% and decrease at higher TOC (>5%; Figure 6a). We also observed comparable trends between layer-specified S1 and S2 values and whole-rock TOC contents (Figure 6b,c). Notably, in the higher layer-specific TOC, S1 and S2 values are found in the lower (2.80 wt.%, 0.45 mg/g, and 18.2 mg/g on average) and middle layers (3.96 wt.%, 0.57 mg/g, and 26.2 mg/g on average), while the lowest values are detected in the upper layer (1.66 wt.%, 0.17 mg/g, and 11.8 mg/g on average) (Table 1). This highlights the contribution of middle and lower layers to whole-rock organic parameters.

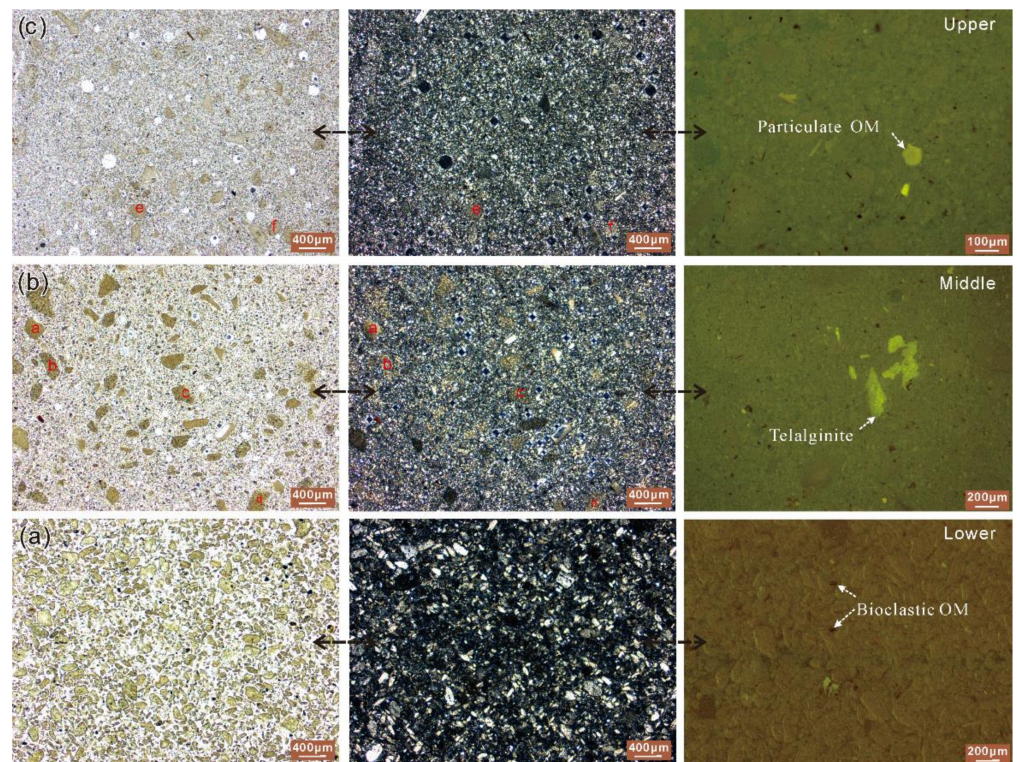


Figure 5. Features of thin section and polished section for lower (a), middle (b), and upper layers (c) in low-mature oil shales (Sample S50), showing photographs of thin sections with plane (−) and perpendicular (+) polarized light, and polished sections with fluorescent light.

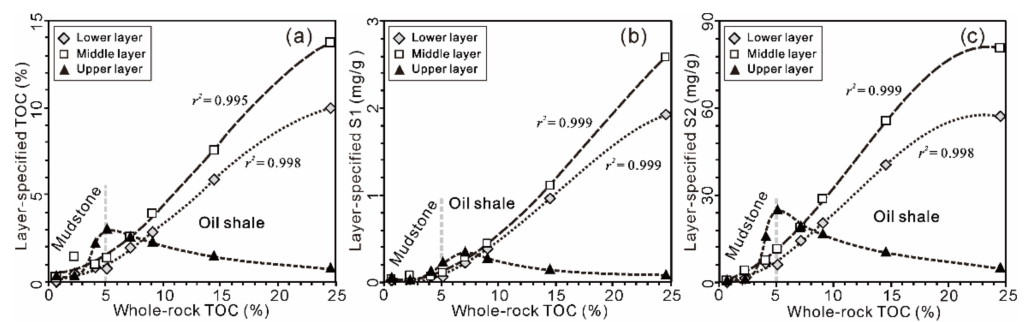


Figure 6. Correlations between whole-rock TOC contents and values of layer-specified TOC (a), layer-specified S1 (b), and layer-specified S2 (c).

3.4. Thermal Variation of OM and Mineral

3.4.1. TG-DSC Analysis

The TG-DSC analysis can be used to determine loss weights by TG curves (Figure 7a,b) and their products (e.g., water, OM) by DSC curves (Figure 7c) at different heating stages [49]. Three stages of loss weights from oil shales and mudstones are observed at less than 150 °C (stage I), 300–550 °C (stage II), and 600–750 °C (stage III) (Figure 7a,b), respectively. An obvious loss weight is detected in stage II (4.0–28.5 wt.%) compared to stages I (2.4–3.1 wt.%) and III (0–3.8 wt.%) (Figure 7a,b). Moreover, loss weights at stage II show a good correlation with TOC contents in all samples ($r^2 = 0.999$; Figure 7d), whereas there are almost no correlations between loss weights and TOC contents at stages I and III (Figure 7d). The fastest loss weights occur at 457 °C for all samples (Figure 7b). Different peaks of loss weights correspond to the process of exothermic oxidation and endothermic dehydration with various OM and water (Figure 7c). Multiple endothermic valleys and exothermic processes are observed during the heating process (Figure 7c).

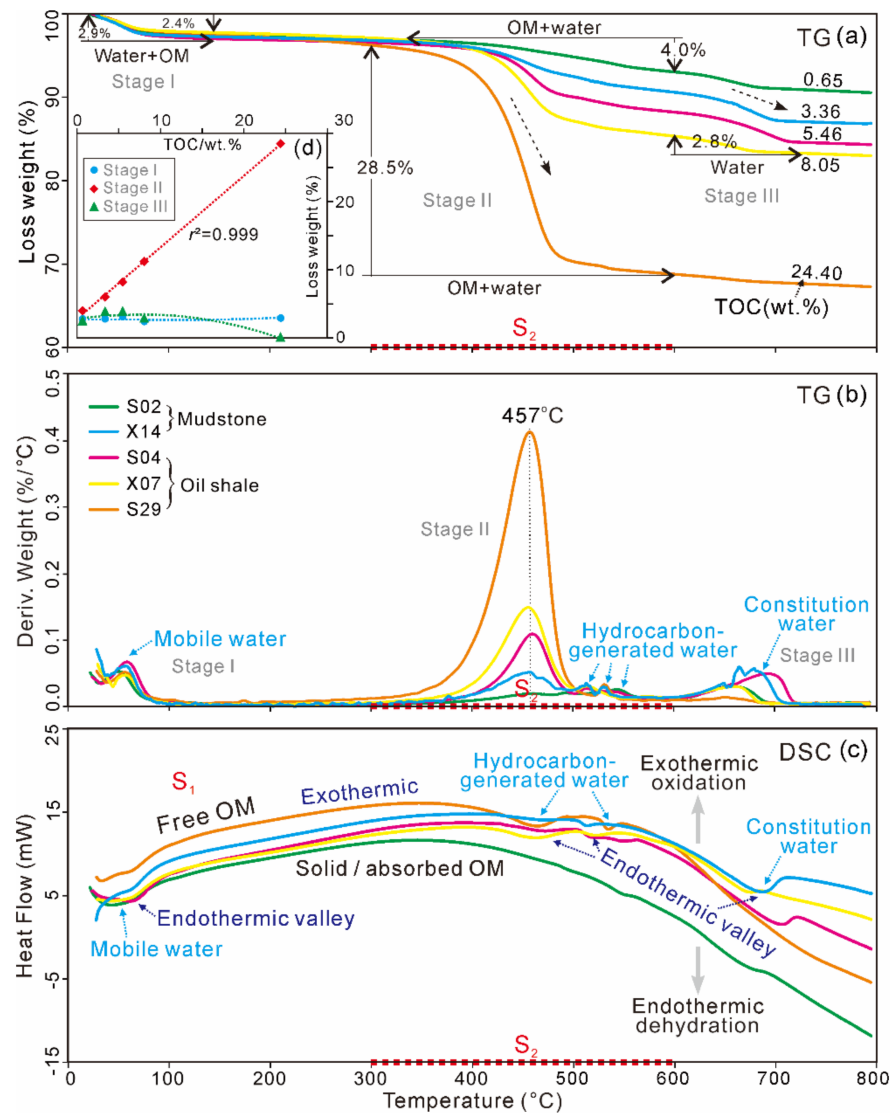


Figure 7. The curve distribution of loss weight (a) and derivative weight (b) from thermogravimetry (TG), heat flow from differential scanning calorimetry (DSC) (c), plot of TOC and loss weight (d) for oil shales and mudstones in boreholes Ngn2 and ZK3389 (after [49]).

3.4.2. Changes in Mineral Phases

The mineral composition of oil shales and mudstones in the K_2qn_1 is characterized by quartz and feldspar, clay mineral, carbonate mineral, and heavy mineral [9]. The clay minerals contain smectite (4.8–43.3%, avg. 26.4%), mixed-layer illite/smectite (I/S) (30.2–43.9%, avg. 35.5%), illite (12.2–32.5%, avg. 24.1%), chlorite (5.7–25.2%, avg. 11.5%), and kaolinite (0.7–6.3%, avg. 2.4%) (Figure 8a–d). The I/S (avg. 37.6%) and illite (avg. 28.4%) minerals dominate in mudstones (Figure 8a,b), whereas preponderant smectite (avg. 39.6%) and I/S contents (avg. 33.5%) are detected in oil shales (Figure 8c,d). In addition, various clay minerals exhibit different thermal responses for mudstones and oil shales (Figure 8). The I/S (1.05–1.28 nm) and chlorite (0.71 nm, 1.42 nm) minerals at over 450 °C are almost converted to illite (1.0 nm) (Figure 8a–d). However, there are almost no changes in clay minerals at the lower temperature (<200 °C) for all samples (Figure 8a–d). A distinct smectite peak occurs in oil shales after ethylene glycol-saturated samples (Figure 8c,d).

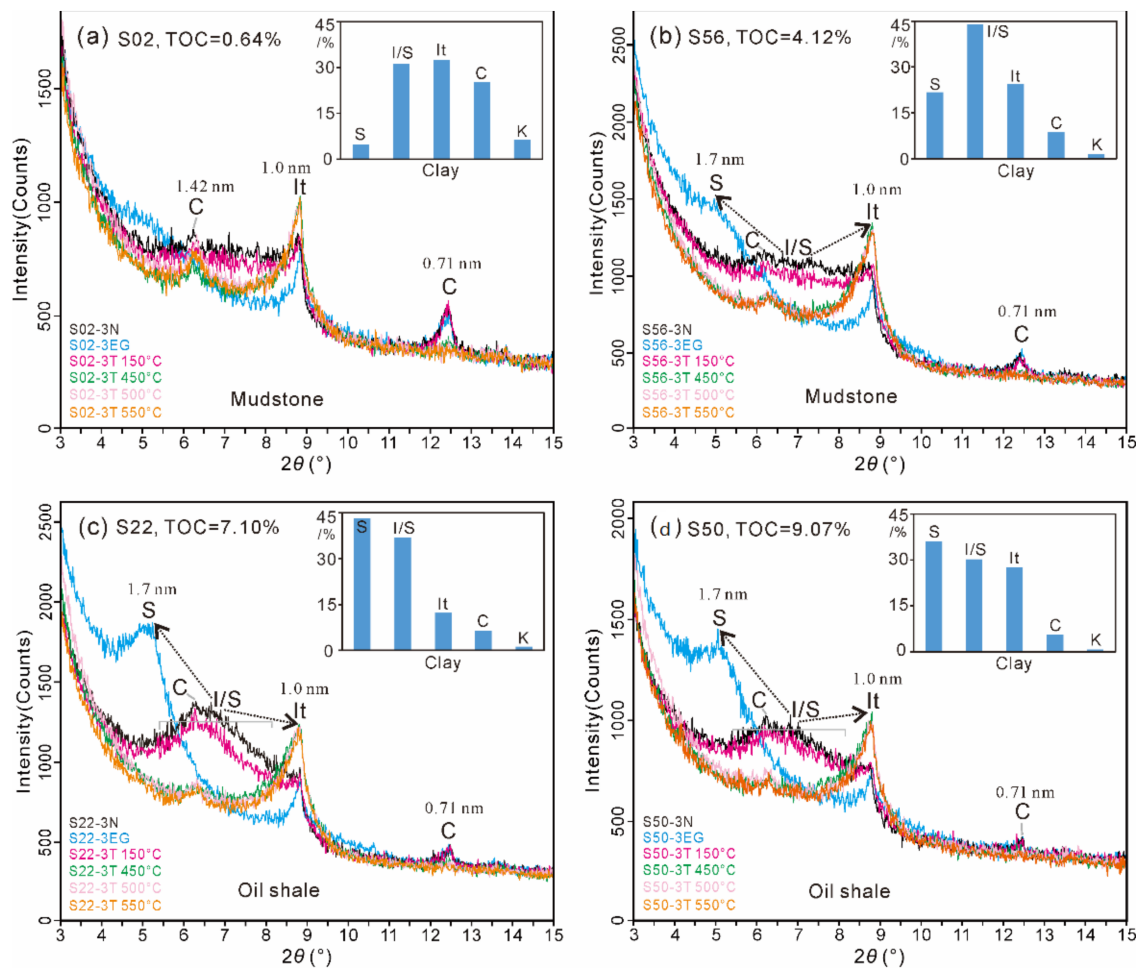


Figure 8. XRD patterns with mineral contents from selective clay minerals of oil shales and mudstones by various heat treatments, including natural oriented (N), ethylene glycol-saturated (EG), and high temperature (T 150 °C, T 450 °C, T 500 °C, and T 550 °C), exhibiting samples S02 (a), S56 (b), S22 (c), and S50 (d) in the K_2qn_1 .

3.4.3. Changes in *N*-Alkane Distribution

The high amounts of *n*-alkanes, steroides, and hopanoids are detected in the total ion chromatograms of the saturated hydrocarbon fractions of oil shales in K_2qn_1 and K_2n_{1-2} intervals (Figure 9a). The *n*-alkanes are characterized by a high abundance of *n*-alkanes of intermediate chain length (C_{21-25}) (avg. 0.40) and long chain ($>n-C_{27}$) (avg. 0.28) components (Figure 9a). Further obvious differences are indicated by the *n*-alkane distribution (Figure 9b). In general, the *n*-alkane distribution patterns (m/z 85) are characterized by microalgal and phytoplankton origins with terrestrial plants in lacustrine oil shales [45–47]. The oil shales of K_2qn_1 and K_2n_{1-2} intervals show high relative proportions of short- (C_{15-19}) to mid-chain *n*-alkanes (C_{21-25}) (avg. 0.54) compared to long chain *n*-alkanes ($>n-C_{27}$) (avg. 0.28) with a low carbon preference index (CPI~1.5) (Figure 9b), indicating a major contribution of aquatic organisms to oil shale deposits. However, a visibly increased abundance in C_{1-5} (avg. 0.43) to C_{6-14} *n*-alkanes (avg. 0.31) compared with that of C_{15+} *n*-alkanes (avg. 0.25) is detected in the pyrolysis gas chromatogram (600 °C) (Figure 9c).

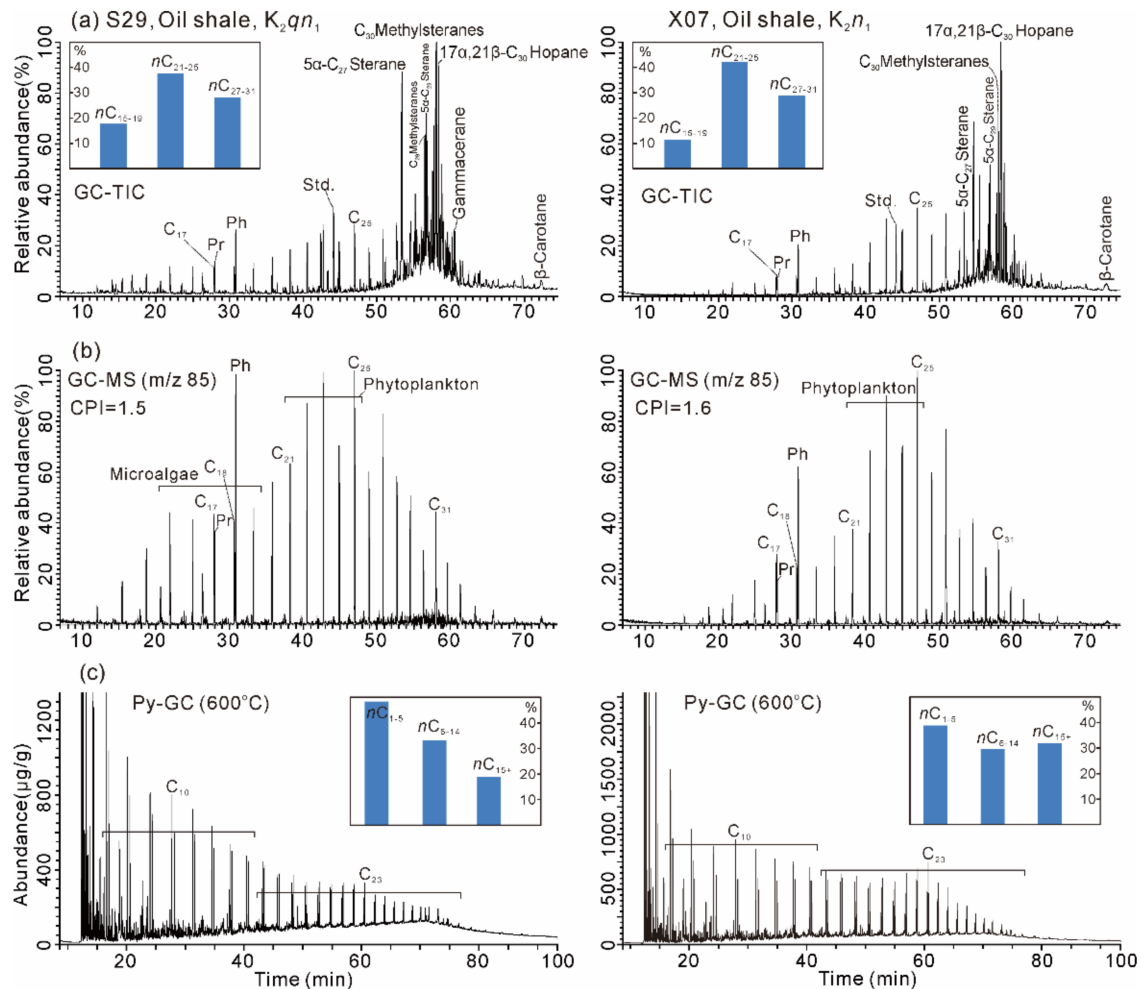


Figure 9. *n*-alkane distributions and their contents from gas chromatograms (TIC) (a), gas chromatograms-mass chromatograms (GC-MS) (m/z 85) (b), pyrolysis-gas chromatography (Py-GC) (c) of saturated hydrocarbon fractions for oil shale samples S29 from the K_2q_{n1} , and X07 from the K_2n_1 .

4. Discussion

The association between OM and minerals plays an important role in influencing the hydrocarbon-generated process during the sedimentation and diagenesis of lacustrine oil shales. The data obtained in this study allow us to explore the formation of particle-size distributions and thermal variation related to various OM and minerals.

4.1. Particle-Size Distribution Associated with OM Occurrence

OM occurrences have been broadly investigated for carbon preservation, carbon cycle and carbon distribution in soils, marine sediments, and lacustrine shales [50–53]. In this study, the settling fractionation and laser particle analyses were employed to explore the particle-size distribution associated with OM occurrence in oil shales and mudstones (Figures 2–6). In general, OM in source rocks can be divided into insoluble OM and soluble OM [54,55], and soluble OM is composed of mobile OM and stable OM [56,57].

Based on the settling result, the lower layer is composed of bioclastic OM (e.g., plant debris, isolated algae) mixed with the detrital mineral (Figure 5a), while the middle layer is made of a mineral surface associated OM by physical adsorption that forms larger particles and OM adsorbed on mineral surfaces (Figure 5b). The upper layer, identified as the most studied clay-sized fractions [1], consists of chemical adsorbed OM in clay interlayers that forms fine particles (Figure 5c) [35]. Arguably, granular OM coexists with detrital minerals in coarse grains, while soluble OM combines with clay minerals in fine grains [20,58]. In

general, the physical adsorption is attained by the intermolecular attraction resulting in OM hosting in mineral surface pores [59], whereas the remaining net charges due to ion substitution or hydrolysis contribute to the chemical adsorption of OM into the mineral surface and interlayer [17].

The particle-size abundance of fine grains (<1 μm) increased in mudstone (TOC < 5.0 wt.%) and then decreased in oil shales (TOC > 5.0 wt.%) (Figure 4a). This leads to an enhanced contribution in mudstones and then reduced contribution in oil shales from clay-adsorbed OM of fine particles to whole-rock TOC (upper layer; Figure 6a). Meanwhile, the particle-size abundance decreased in medium grains (1–20 μm) and increased in coarse grains (>20 μm) with increasing TOC contents (Figure 4a). This implies that OM polymerization affects the change in the distribution of particle sizes for oil shales and mudstones. Some potential organic-clay aggregates could be observed in the middle and upper layers by thin sections (Figure 5b,c). In addition, mineral-surface-associated OM (middle layer) and bioclastic OM (lower layer) contribute to whole-rock TOC of oil shale (Figure 6a). We infer that the difference of OM occurrences in oil shales and mudstones could be concerned with the depositional environment.

4.2. Influence of Depositional Environment on OM Occurrence

In the depositional environment, the primary organism and its exposure to oxygen (oxidation) control the extent and preservation state of OM in sedimentary rocks [60]. In this study, OM occurrences may reflect the different degrees of oxidation of the primary organism during sedimentary and burial processes.

Low TOC contents (<5%) in mudstone intervals suggest that oxygen is present in the water column, leading to a longer exposure time during the settling of particulate OM [45–47], resulting in the primary organism to be oxidized and decomposed into plenty of particulate OM and even soluble OM. Thus, higher settling rates of particulate OM adsorbed on mineral surfaces favor the enhanced preservation of mineral-associated OM (middle layer; Figure 6c) [16,60], leading to increased mineral-associated OM and decreased bioclastic OM (lower layer; Figure 6c). In particular, the chemical adsorption of abundant soluble OM to the increased clay surface forms the increase of clay interlayer-sorbed OM (upper layer; Figure 6c) [8].

High TOC contents (>5%) in oil shale intervals presume an oxygen-deficient water column [45–47] and a shorter oxygen exposure time for the degradation of OM [61], resulting in increased bioclastic OM and reduced mineral-associated OM (Figure 6) [16]. The enhanced microbial degradation [45–47] contributes to the increase in free OM (Figure 6b). However, the generation of clay interlayer-sorbed OM is greatly restrained (upper layer; Figure 6c), because of reduced oxygenolysis of the primary organism in an anoxic water condition during the oil shale deposition [45,46]. Therefore, once associated with minerals (middle and upper layer; Figure 6c), the OM can become resistant to microbial degradation, leading to efficient OM preservation [62,63].

Arguably, various types of OM occurrences are influenced by the abundance of OM sources and redox conditions in the lake water, whereas the degree of biodecomposition and its particle sizes would affect the place of OM occurrences. Our results provide some clues that the clay surface and interlayers are primary places for small-sized OM under suboxic conditions in mudstones, while granular OM mainly hosted in the mineral surface under anoxic conditions in oil shales.

4.3. Synchronous Response of OM and Minerals to Thermal Variation

In this study, TG-DSC, heated XRD, and Py-GC analyses [14,25,30] were employed to investigate decomposition processes and decomposed products of oil shales and mudstones in the pyrolysis (Figures 7–9). Based on TG-DSC curves of oil shales and mudstones, we observe three stages of loss weights at less than 150 °C, 300–550 °C, and 600–750 °C (Figure 7a,b), respectively. This process could be accompanied by OM decomposition, mineral transformation, and water release from oil shales and mudstones [14,38].

During the low temperature (<300 °C), free OM corresponding to S1 because of their similar release of temperatures obtained from Rock-Eval pyrolysis and TG-DSC curves, confirmed by an exothermic process, was expelled with mobile water by an endothermic process (Figure 7a–c). This is also confirmed by recent findings from retorting experiments [32]. However, there are almost no changes in clay minerals at a lower temperature (<200 °C) for all samples (Figure 8a–d). At the range of 300 to 550 °C, a continuous exothermic process implies the release of other types of OM (e.g., solid and absorbed OMs) corresponding to S2 (Figure 7a–c) [38], and abundant OM from oil shales was not expelled until the temperature reached 550 °C (Figure 7a,b). This result is in agreement with that a large amount of oil from oil shales that was produced at 300–475 °C by retorting experiments [32]. Meanwhile, the type and abundance of clay minerals (e.g., I/S, chlorite) at over 450 °C occur in variations as a drifting characteristic peak (Figure 8a–d). The I/S and chlorite minerals at over 450 °C are almost converted to illite (Figure 8a–d). This is also confirmed by the heating XRD of clay minerals [14]. Then, large amounts of hydrocarbon-generated water with an endothermic process were expelled in the following, due to the pyrolysis of abundant OM for oil shales (Figure 7b,c). In addition, the visibly endothermic valleys with loss weights occurred in a higher temperature (600–750 °C) (Figure 7b,c), due to the loss of constitution water from clay mineral lattices (e.g., smectite, chlorite; Figure 8) [14]. For the molecular scale, we observe a predominant abundance in C_{1–5} to C_{6–14} *n*-alkanes (avg. 0.74) of the Py-GC (600 °C) pyrolyzed from short- to mid-chain *n*-alkanes (C_{15–25}) (avg. 0.54) of the GC (Figure 9a,c), indicating strong pyrolysis at a high temperature for longer chain *n*-alkanes in oil shales [64].

Consequently, a synchronous response of OM and minerals to thermal variation dominates at 300–550 °C for oil shales and mudstones. The I/S and chlorite minerals are characterized by remarkable illitization, while solid and absorbed OMs and hydrocarbon-generated water were expelled in large quantities. This contributes to the major loss weights of oil shale and mudstone in K₂qn₁ and K₂n_{1–2} intervals during the heating process.

4.4. Implication for Hydrocarbon-Generated Process

Associations between minerals and OM can be directly observed by SEM-BSE micrographs combined with energy dispersive spectroscopy [18,35]. The amorphous OM in oil shales is encapsulated by clay minerals forming clay-organic nanocomposites, confirmed by the growth of lamalginite [9]. Meanwhile, isolated OM is surrounded by diagenetic quartz and clays [45]. Hence, the placement of OM occurrences is closely related to minerals in oil shales. More critically, the synchronous process of OM decomposition and mineral transformation occurs at 300–550 °C for oil shales and mudstones (Figures 7 and 8). This also exists in the process of OM thermal evolution or the in-situ production for oil shales [29–34,42,43], contributing to exploring the hydrocarbon-generated process of oil shales.

The peak hydrocarbon-generated rate with the fastest loss weights occurred at approximately 457 °C for oil shales and mudstones in K₂qn₁ and K₂n_{1–2} intervals (Figure 7b), corresponding to maturity to high maturity around 1.3% vitrinite reflectance value [65]. This is consistent with the pyrolysis of Estonia, Green River, and Huadian oil shales [29,33,36]. A further productivity analysis shows that the best temperature for the in-situ pyrolysis of oil shales is about 500 °C [26]. This result is important for revealing the dynamic process of hydrocarbon generation. However, relatively high PI values (>0.05) occur around 435 °C (T_{max}) with low maturity (Figure 10a), which is linked to the relationship between hydrocarbon generation potential and thermal maturity [42]. Except for hydrocarbon generation by oxidation during mudstone deposition (Figure 10a), the catalytic hydrocarbon generation by clay minerals plays an important role in the formation of low-mature shale oil and gas [19]. Further evidence comes from the synchronous response of OM and minerals to thermal variation for oil shales and mudstones (Figures 7 and 8). In addition, oil shales developed in an anoxic lacustrine environment [45,46] present an overall higher degradation ratio (PC/TOC > 60%) compared with that of mudstones (Figure 10b), indicating an enhanced efficiency of hydrocarbon generation for oil shales. This could be closely related

to the OM occurrence of oil shales. Certainly, the high degradation ratio for oil shales in K_2qn_1 and K_2n_{1-2} intervals (Figure 10b) is verified for a huge potential for the in-situ exploitation of oil shales.

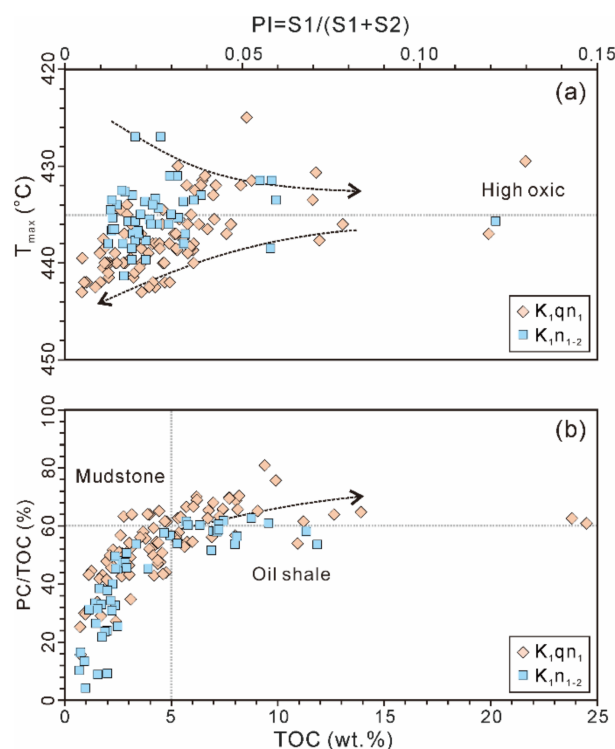


Figure 10. Plots of PI and T_{max} (a), TOC and PC/TOC (b) for oil shales and mudstones in the K_2qn_1 and K_2n_{1-2} . Partial data of TOC and PC/TOC in the K_2qn_1 are from [49].

This study illustrates the importance of examining the OM occurrence and thermal degradation to interpret the hydrocarbon-generated process of lacustrine oil shales, which contributes to shale oil and gas exploration in similar depositional settings. OM associated with minerals may have potential implications for the hydrocarbon generation potential of oil shales and its in-situ exploitation.

5. Conclusions

Low-mature (425–443 °C T_{max}) oil shales with high TOC contents (5.13–24.51 wt.%) were developed in the Songliao Basin, depositing in a semi-deep to deep lacustrine environment during the K_2qn_1 and K_2n_{1-2} periods. After the settling of the particles from oil shales and mudstones in the water column, three layers are characterized by a distinct color, degree of consolidation, and particle size. Meanwhile, the size of powder particles is divided into three ranges of fine grain (<1 μm), medium grain (1–20 μm), and coarse grain (>20 μm), in which the abundance of medium grains dominates. The particle-size abundance of fine grains increased in mudstones and then decreased in oil shales, while the particle-size abundance decreased in medium grains and increased in coarse grains with increasing TOC contents. This implies that OM polymerization affects the change in the distribution of particle sizes for oil shales and mudstones, and the mineral-surface-associated and bioclastic OMs contribute to the whole-rock TOC of oil shale.

The difference of OM occurrences in oil shales and mudstones could be concerned with the depositional environment. Various types of OM occurrences are influenced by the abundance of OM sources and redox conditions, whereas the degree of biodecomposition and its particle sizes would affect the placement of OM occurrences. Furthermore, a synchronous response of OM and minerals to thermal variation dominates at 300–550 °C for oil shales and mudstones. The I/S and chlorite minerals are characterized by remarkable

illitization, while solid and absorbed OMs and hydrocarbon-generated water were expelled in large quantities. This contributes to the major loss weights of oil shale and mudstone during the heating process. The peak hydrocarbon-generated rate occurred at 457 °C for oil shales, corresponding to maturity to high maturity around 1.3% vitrinite reflectance value. This study reveals the important role played by OM occurrence and thermal degradation in the hydrocarbon-generated process of oil shales. However, the role of clay minerals in the catalytic hydrocarbon generation of oil shales is still unclear. Further research would focus on the effect of OM and minerals' association on the in-situ exploitation of oil shales.

Author Contributions: Conceptualization, Funding acquisition, Investigation, Methodology, Project administration, Writing—Original draft, J.J.; Writing—review and editing, Z.L. All authors have read and agreed to the published version of the manuscript.

Funding: This study is supported by the National Natural Science Foundation of China (No. 41772114, 41402123) and the China Postdoctoral Science Foundation (No. 2016T90255).

Institutional Review Board Statement: Not applicable.

Informed Consent Statement: Not applicable.

Acknowledgments: We thank Pingchang Sun, Jianpeng Wang, and Shuqing Yao for assistance in core logging and sampling and Reinhard F. Sachsenhofer, Achim Bechtel, Susanne A.I. Strobl, Yuan Gao, and Ping Li for help in sample analysis and discussion. We acknowledge Academic Editor and Assistant Editor, and constructive criticism from four anonymous reviewers that greatly improved this manuscript.

Conflicts of Interest: The authors declare no conflict of interest.

References

1. Zhu, X.; Cai, J.; Liu, W.; Lu, X. Occurrence of stable and mobile organic matter in the clay-sized fraction of shale: Significance for petroleum geology and carbon cycle. *Int. J. Coal Geol.* **2016**, *160–161*, 1–10. [[CrossRef](#)]
2. Keil, R.; Hedges, J. Sorption of organic matter to mineral surfaces and the preservation of organic matter in coastal marine sediments. *Chem. Geol.* **1993**, *107*, 385–388. [[CrossRef](#)]
3. Keil, R.G.; Tsamakis, E.; Fuh, C.; Giddings, J.; Hedges, J.I. Mineralogical and textural controls on the organic composition of coastal marine sediments: Hydrodynamic separation using SPLITT-fractionation. *Geochim. Cosmochim. Acta* **1994**, *58*, 879–893. [[CrossRef](#)]
4. Kell, R.G.; Montluçon, D.B.; Prahli, F.G. Sorptive preservation of labile organic matter in marine sediments. *Nature* **1994**, *370*, 549–552. [[CrossRef](#)]
5. Mayer, L.M. Surface area control of organic carbon accumulation in continental shelf sediments. *Geochim. Cosmochim. Acta* **1994**, *58*, 1271–1284. [[CrossRef](#)]
6. Bergamaschi, B.; Tsamakis, E.; Keil, R.G.; Eglinton, T.I.; Montluçon, D.B.; Hedges, J.I. The effect of grain size and surface area on organic matter, lignin and carbohydrate concentration, and molecular compositions in Peru Margin sediments. *Geochim. Cosmochim. Acta* **1997**, *61*, 1247–1260. [[CrossRef](#)]
7. Hedges, J.I.; Keil, R.G. Sedimentary organic matter preservation: An assessment and speculative synthesis. *Mar. Chem.* **1995**, *49*, 81–95. [[CrossRef](#)]
8. Kennedy, M.J.; Pevear, D.R.; Hill, R.J. Mineral surface control of organic carbon in black shale. *Science* **2002**, *295*, 657–660. [[CrossRef](#)] [[PubMed](#)]
9. Jia, J.; Liu, Z.; Zhou, R.; Liu, R.; Gao, Y. Variation in pore space and structure of organic-rich oil-prone shales from a non-marine basin: Constraints from organic matter and minerals. *Acta Geol. Sin.* **2021**, online. [[CrossRef](#)]
10. Mayer, L. Extent of coverage of mineral surfaces by organic matter in marine sediments. *Geochim. Cosmochim. Acta* **1999**, *63*, 207–215. [[CrossRef](#)]
11. Dexter, A.; Richard, G.; Arrouays, D.; Czyż, E.A.; Jolivet, C.; Duval, O. Complexed organic matter controls soil physical properties. *Geoderma* **2008**, *144*, 620–627. [[CrossRef](#)]
12. Hedges, J.I.; Keil, R.G. Organic geochemical perspectives on estuarine processes: Sorption reactions and consequences. *Mar. Chem.* **1999**, *65*, 55–65. [[CrossRef](#)]
13. Mayer, L.M.; Schick, L.L.; Hardy, K.R.; Wagai, R.; McCarthy, J. Organic matter in small mesopores in sediments and soils. *Geochim. Cosmochim. Acta* **2004**, *68*, 3863–3872. [[CrossRef](#)]
14. Cai, J.G.; Bao, Y.J.; Yang, S.Y.; Wang, X.X.; Fan, D.D.; Xu, J.L.; Wang, A.P. Research on preservation and enrichment mechanisms of organic matter in muddy sediment and mudstone. *Sci. China Ser. D Earth Sci.* **2007**, *50*, 765–775. [[CrossRef](#)]
15. Lopez-Sangil, L.; Rovira, P. Sequential chemical extractions of the mineral associated soil organic matter: An integrated approach for the fractionation of organo-mineral complexes. *Soil Biol. Biochem.* **2013**, *62*, 57–67. [[CrossRef](#)]

16. Arnarson, T.S.; Keil, R.G. Changes in organic matter–mineral interactions for marine sediments with varying oxygen exposure times. *Geochim. Cosmochim. Acta* **2007**, *71*, 3545–3556. [[CrossRef](#)]
17. Arnarson, T.S.; Keil, R.G. Mechanisms of pore water organic matter adsorption to montmorillonite. *Mar. Chem.* **2000**, *71*, 309–320. [[CrossRef](#)]
18. Kennedy, M.J.; Löhr, S.C.; Fraser, S.A.; Baruch, E.T. Direct evidence for organic carbon preservation as clay-organic nanocomposites in a Devonian black shale: From deposition to diagenesis. *Earth Planet Sc. Lett.* **2014**, *388*, 59–70. [[CrossRef](#)]
19. Guan, P.; Xu, Y.; Liu, W. Diverse occurrence and quantitative evaluation of organic matter in petroleum source rocks. *Sci. Bull.* **1998**, *43*, 1556–1559.
20. Cai, J.; Xu, J.; Yang, S.; Bao, Y.; Lu, L. The fractionation of an argillaceous sediment & difference in organic matter enrichment in different fractions. *Geol. J. China Univ.* **2006**, *12*, 234–241.
21. Brendow, K. Global oil shale issues and perspectives. *Oil Shale* **2003**, *20*, 81–92.
22. Liu, Z.; Meng, Q.; Dong, Q.; Zhu, J.; Guo, W.; Ye, S.; Liu, R.; Jia, J. Characteristics and resource potential of oil shale in China. *Oil Shale* **2017**, *34*, 15. [[CrossRef](#)]
23. Palci, F.; Fraser, A.J.; Neumaier, M.; Goode, T.; Parkin, K.; Wilson, T. Shale oil and gas resource evaluation through 3D basin and petroleum systems modelling: A case study from the East Midlands, onshore UK. *Pet. Geosci.* **2020**, *26*, 525–543. [[CrossRef](#)]
24. Zhao, W.; Hu, S.; Hou, L.; Yang, T.; Li, X.; Guo, B.; Yang, Z. Types and resource potential of continental shale oil in China and its boundary with tight oil. *Pet. Explor. Dev.* **2020**, *47*, 1–11. [[CrossRef](#)]
25. Sun, Y.-H.; Bai, F.-T.; Lü, X.-S.; Li, Q.; Liu, Y.-M.; Guo, M.-Y.; Guo, W.; Liu, B. A novel energy-efficient pyrolysis process: Self-pyrolysis of oil shale triggered by topochemical heat in a horizontal fixed bed. *Sci. Rep.* **2015**, *5*, 8290. [[CrossRef](#)]
26. Zhao, S.; Li, Q.; Lü, X.; Sun, Y. Productivity analysis of fuyu oil shale in-situ pyrolysis by injecting hot nitrogen. *Energies* **2021**, *14*, 5114. [[CrossRef](#)]
27. Han, Y.; Horsfield, B.; Mahlstedt, N.; Wirth, R.; Lareau, H. Factors controlling source and reservoir characteristics in the Niobrara shale oil system, Denver Basin. *AAPG Bull.* **2019**, *103*, 2045–2072. [[CrossRef](#)]
28. En, A.; Kozlu, H. Impact of maturity on producible shale oil volumes in the Silurian (Llandovery) hot shales of the northern Arabian plate, southeastern Turkey. *AAPG Bull.* **2020**, *104*, 507–524. [[CrossRef](#)]
29. Maaten, B.; Loo, L.; Konist, A.; Siirde, A. Mineral matter effect on the decomposition of Ca-rich oil shale. *J. Therm. Anal. Calorim.* **2017**, *131*, 2087–2091. [[CrossRef](#)]
30. Bai, F.; Liu, Y.; Lai, C.; Sun, Y.; Wang, J.; Sun, P.; Xue, L.; Zhao, J.; Guo, M. Thermal degradations and processes of four kerogens via thermogravimetric–fourier-transform infrared: Pyrolysis performances, products, and kinetics. *Energ. Fuel* **2020**, *34*, 2969–2979. [[CrossRef](#)]
31. Pikkor, H.; Maaten, B.; Baird, Z.S.; Jrvik, O.; Lees, H. Surface area of oil shale and its solid pyrolysis products depending on the particle size. *Chem. Eng. Trans.* **2020**, *81*, 961–966. [[CrossRef](#)]
32. Yu, F.; Sun, P.; Zhao, K.; Ma, L.; Tian, X. Experimental constraints on the evolution of organic matter in oil shales during heating: Implications for enhanced in situ oil recovery from oil shales. *Fuel* **2019**, *261*, 116412. [[CrossRef](#)]
33. Yan, J.; Jiang, X.; Han, X.; Liu, J. A TG–FTIR investigation to the catalytic effect of mineral matrix in oil shale on the pyrolysis and combustion of kerogen. *Fuel* **2013**, *104*, 307–317. [[CrossRef](#)]
34. Du, J.; Cai, J.; Lei, T.; Li, Y. Diversified roles of mineral transformation in controlling hydrocarbon generation process, mechanism, and pattern. *Geosci. Front.* **2020**, *12*, 725–736. [[CrossRef](#)]
35. Löhr, S.; Kennedy, M. Organomineral nanocomposite carbon burial during Oceanic Anoxic Event 2. *Biogeosciences* **2014**, *11*, 4971–4983. [[CrossRef](#)]
36. Burnham, A.; Huss, E.B.; Singleton, M.F. Pyrolysis kinetics for Green River oil shale from the saline zone. *Fuel* **1983**, *62*, 1199–1204. [[CrossRef](#)]
37. Vandenbroucke, M.; Largeau, C. Kerogen origin, evolution and structure. *Org. Geochem.* **2007**, *38*, 719–833. [[CrossRef](#)]
38. Ding, F.; Cai, J.; Song, M.; Yuan, P. The relationship between organic matter and specific surface area in <2 μm clay size fraction of muddy source rock. *Sci. China Earth Sci.* **2013**, *56*, 1343–1349. [[CrossRef](#)]
39. Bu, H.; Yuan, P.; Liu, H.; Liu, D.; Liu, J.; He, H.; Zhou, J.; Song, H.; Li, Z. Effects of complexation between organic matter (OM) and clay mineral on OM pyrolysis. *Geochim. Cosmochim. Acta* **2017**, *212*, 1–15. [[CrossRef](#)]
40. Liu, H.; Yuan, P.; Liu, D.; Bu, H.; Song, H.; Qin, Z.; He, H. Pyrolysis behaviors of organic matter (OM) with the same alkyl main chain but different functional groups in the presence of clay minerals. *Appl. Clay Sci.* **2018**, *153*, 205–216. [[CrossRef](#)]
41. Zhu, X.; Cai, J.; Wang, Y.; Liu, H.; Zhang, S. Evolution of organic–mineral interactions and implications for organic carbon occurrence and transformation in shale. *GSA Bull.* **2019**, *132*, 784–792. [[CrossRef](#)]
42. Haile, B.G.; Klausen, T.G.; Jahren, J.; Braathen, A.; Hellevang, H. Thermal history of a triassic sedimentary sequence verified by a multi-method approach: Edgeøya, Svalbard, Norway. *Basin Res.* **2018**, *30*, 1075–1097. [[CrossRef](#)]
43. Manganot, X.; Deçoninck, J.-F.; Bonifacie, M.; Rouchon, V.; Collin, P.-Y.; Quesne, D.; Gasparrini, M.; Sizun, J.-P. Thermal and exhumation histories of the northern subalpine chains (Bauges and Bornes-France): Evidence from forward thermal modeling coupling clay mineral diagenesis, organic maturity and carbonate clumped isotope (Δ47) data. *Basin Res.* **2018**, *31*, 361–379. [[CrossRef](#)]
44. Feng, Z.; Jia, C.; Xie, X.; Zhang, S.; Feng, Z.; Timothy, A.C. Tectonostratigraphic units and stratigraphic sequences of the nonmarine Songliao Basin, Northeast China. *Basin Res.* **2010**, *22*, 79–95. [[CrossRef](#)]

45. Jia, J.; Bechtel, A.; Liu, Z.; Strobl, S.A.; Sun, P.; Sachsenhofer, R. Oil shale formation in the Upper Cretaceous Nenjiang Formation of the Songliao Basin (NE China): Implications from organic and inorganic geochemical analyses. *Int. J. Coal Geol.* **2013**, *113*, 11–26. [[CrossRef](#)]
46. Jia, J.; Liu, Z.; Bechtel, A.; Strobl, S.A.; Sun, P. Tectonic and climate control of oil shale deposition in the Upper Cretaceous Qingshankou Formation (Songliao Basin, NE China). *Int. J. Earth Sci.* **2013**, *102*, 1717–1734. [[CrossRef](#)]
47. Bechtel, A.; Jia, J.; Strobl, S.A.; Sachsenhofer, R.; Liu, Z.; Gratzner, R.; Püttmann, W. Palaeoenvironmental conditions during deposition of the Upper Cretaceous oil shale sequences in the Songliao Basin (NE China): Implications from geochemical analysis. *Org. Geochem.* **2012**, *46*, 76–95. [[CrossRef](#)]
48. Gratzner, R.; Bechtel, A.; Sachsenhofer, R.F.; Linzer, H.-G.; Reischenbacher, D.; Schulz, H.-M. Oil–oil and oil–source rock correlations in the Alpine Foreland Basin of Austria: Insights from biomarker and stable carbon isotope studies. *Mar. Pet. Geol.* **2011**, *28*, 1171–1186. [[CrossRef](#)]
49. Jia, J.; Liu, Z.; Meng, Q.; Sun, P.; Xu, J.; Liu, R.; Bai, Y. Response mechanism between oil yield and total organic carbon of nonmarine oil shale in China. *J. Jilin Univ. Earth Sci. Ed.* **2020**, *50*, 368–377.
50. Torn, M.; Trumbore, S.E.; Chadwick, O.A.; Vitousek, P.M.; Hendricks, D.M. Mineral control of soil organic carbon storage and turnover. *Nature* **1997**, *389*, 170–173. [[CrossRef](#)]
51. Mikutta, R.; Kleber, M.; Torn, M.S.; Jahn, R. Stabilization of soil organic matter: Association with minerals or chemical recalcitrance? *Biogeochemistry* **2006**, *77*, 25–56. [[CrossRef](#)]
52. Kennedy, M.J.; Wagner, T. Clay mineral continental amplifier for marine carbon sequestration in a greenhouse ocean. *Proc. Natl. Acad. Sci.* **2011**, *108*, 9776–9781. [[CrossRef](#)] [[PubMed](#)]
53. Solomon, D.; Lehmann, J.; Harden, J.; Wang, J.; Kinyangi, J.; Heymann, K.; Karunakaran, C.; Lu, Y.; Wirick, S.; Jacobsen, C. Micro- and nano-environments of carbon sequestration: Multi-element STXM–NEXAFS spectromicroscopy assessment of microbial carbon and mineral associations. *Chem. Geol.* **2012**, *329*, 53–73. [[CrossRef](#)]
54. Durand, B. *Kerogen-Insoluble Organic Matter from Sedimentary Rocks*; Technip: Paris, France, 1980.
55. Tissot, B.P.; Welte, D.H. *Petroleum Formation and Occurrence*; Springer: New York, NY, USA, 1984.
56. Jeng, W.-L.; Chen, M.-P. Grain size effect on bound lipids in sediments off northeastern Taiwan. *Org. Geochem.* **1995**, *23*, 301–310. [[CrossRef](#)]
57. Garcette-Lepecq, A.; Largeau, C.; Bouloubassi, I.; Derenne, S.; Saliot, A.; Lorre, A.; Point, V. Lipids and their modes of occurrence in two surface sediments from the Danube delta and North-western Black sea: Implications for sources and early diagenetic alternation I: Carboxylic acids. *Org. Geochem.* **2004**, *35*, 959–980. [[CrossRef](#)]
58. Keil, R.G.; Tsamakis, E.; Giddings, J.C.; Hedges, J.H. Biochemical distributions (amino acids, neutral sugars, and lignin phenols) among size classes of modern marine sediments from the Washington coast. *Geochim. Cosmochim. Acta.* **1998**, *62*, 1347–1364. [[CrossRef](#)]
59. Schulte, S.; Mangelsdorf, K.; Rullkötter, J. Organic matter preservation on the Pakistan continental margin as revealed by biomarker geochemistry. *Org. Geochem.* **2000**, *31*, 1005–1022. [[CrossRef](#)]
60. Zimmerman, A.R.; Goynes, K.W.; Chorover, J.; Komarneni, S.; Brantley, S.L. Mineral mesopore effects on nitrogenous organic matter adsorption. *Org. Geochem.* **2004**, *35*, 355–375. [[CrossRef](#)]
61. Hartnett, H.E.; Keil, R.G.; Hedges, J.I.; Devol, A.H. Influence of oxygen exposure time on organic carbon preservation in continental margin sediments. *Nature* **1998**, *391*, 572–575. [[CrossRef](#)]
62. Kaiser, K.; Guggenberger, G. The role of DOM sorption to mineral surfaces in the preservation of organic matter in soils. *Org. Geochem.* **2000**, *31*, 711–725. [[CrossRef](#)]
63. Arnarson, T.S.; Keil, R.G. Influence of organic-mineral aggregates on microbial degradation of the dinoflagellate *Scrippsiella trochoidea*. *Geochim. Cosmochim. Acta* **2005**, *69*, 2111–2117. [[CrossRef](#)]
64. Horsfield, B. Practical criteria for classifying kerogens: Some observations from pyrolysis-gas chromatography. *Geochim. Cosmochim. Acta* **1989**, *53*, 891–901. [[CrossRef](#)]
65. Jia, J.; Wu, Y.; Miao, C.; Fu, C.; Xie, W.; Qin, J.; Wang, X. Tectonic controls on the sedimentation and thermal history of supra-detachment basins: A case study of the early Cretaceous Fuxin Basin, NE China. *Tectonics* **2021**, *40*, e2020TC006535. [[CrossRef](#)]